Late Pleistocene evolution of tides and tidal dissipation

Wilmes, Sophie-Berenice; Pedersen, V. K. ; Schindelegger, Michael; Green, Mattias

Paleoceanography and Paleoclimatology

DOI:
10.1029/2023PA004727

Published: 09/11/2023

Late Pleistocene evolution of tides and tidal dissipation

S.-B. Wilmes[1], V. K. Pedersen[2], M. Schindelegger[3], and J. A. M. Green[1]

[1]School of Ocean Sciences, Bangor University, Bangor, UK
[2]Department of Geoscience, Aarhus University, Aarhus, Denmark
[3]Institute of Geodesy and Geoinformation, University of Bonn, Bonn, Germany

Key Points:

- Tides over the last glacial cycle are explicitly modelled and tidal dissipation ranging back to 430 ka is inferred with regression analysis.
- Enhanced open ocean dissipation (1.8–2.5 $\times$ present day) occurred during glacial maxima, and near-present-day values during interglacials.
- Peak glacial M_2 tidal dynamics are very sensitive to changes in ice sheet extent, which may influence ocean mixing and glacial climate.

Corresponding author: S.-B. Wilmes, `s.wilmes@bangor.ac.uk`

Abstract

Studies of the Last Glacial Maximum (LGM; 26.5–19 ka) tides showed strong enhancements in open ocean tidal amplitudes and dissipation rates; however, changes prior to the LGM remain largely unexplored. Using two different ice sheet and sea level reconstructions, we explicitly simulate the evolution of the leading semi-diurnal and diurnal tidal constituents (M_2, S_2, K_1 and O_1) over the last glacial cycle with a global tide model. Both sets of simulations show that global changes, dominated by the Atlantic, take place for the semi-diurnal constituents, while changes for the diurnal constituents are mainly regional. Irrespective of the reconstruction, open ocean dissipation peaks during the sea level lowstands of MIS 2 ($\sim$20 ka) and MIS 4 ($\sim$60 ka), although dissipation values prior to MIS 2 are sensitive to differences in reconstructed ice sheet extent. Using the statistically significant relationship between global mean sea level and dissipation, we apply regression analysis to infer open ocean and shelf dissipation, respectively, over the last four glacial cycles back to 430 ka. Our analysis shows that open ocean tidal energy was probably increased for most of this period, peaking during glacial maxima, and returning to near-present-day values during interglacials. Due to tidal resonance during glacial phases, small changes in bathymetry could have caused large changes in tidal amplitudes and dissipation, emphasising the need for accurate ice margin reconstructions. During glacial phases, once global mean sea level decreased by more than $\sim$100 m, the amount of open ocean tidal energy available for ocean mixing approximately doubled.

1 Introduction

Tides are important for numerous processes in the ocean: in coastal areas, they shape intertidal ecosystems and morphology. In shelf-sea areas, tidal dynamics determine the location of tidal mixing fronts, which separate seasonally stratified waters from year-round mixed waters (e.g., Simpson & Pingree, 1978). This partitioning is important for shelf sea ecosystems, biogeochemical cycles and the export of CO_2 from the shelf seas to the deep ocean (Thomas et al., 2004). In the open ocean, tidally driven mixing supplies approximately half ($\sim$1 TW) of the energy necessary to sustain the large-scale meridional overturning circulation (Wunsch & Ferrari, 2004; Ferrari & Wunsch, 2009). Recent work (Wilmes et al., 2021) demonstrated that, for the the Last Glacial Maximum (26.5–19 thousand years before present (ka); the LGM hereafter), strong increases in tidal mixing (due to the sea level lowstand and associated changes in tidal dynamics) could be constrained from sediment carbon isotopes. As sea level index points (SLIPs) in coastal areas are generally related to a given high or low tide level and not mean sea level, knowledge of past tidal range changes is important for reconstructing past sea levels (see e.g., Ward et al., 2016). Furthermore, marine terminating ice sheet dynamics are affected by tidal dynamics which influence grounding line movement (Milillo et al., 2017; Batchelor et al., 2023), basal melting (Milillo et al., 2017; Anselin et al., 2023), ice shelf flexure (Walker et al., 2013) and ice flow (Bindschadler et al., 2003; Anandakrishnan, 2003; Gudmundsson, 2007).

Reconstructions of global tides and tidal dissipation during the Quaternary (2.58 Ma to present) have generally focused on the last $\sim$25 thousand years (kyr) encompassing the LGM, the deglacial (19–11.7 ka), and the Holocene (11.7 ka to present) (Egbert et al., 2004; Uehara et al., 2006; Griffiths & Peltier, 2008, 2009; Green, 2010; Wilmes & Green, 2014; Wilmes et al., 2019, 2022; Sulzbach et al., 2023). These investigations showed surprising results: the tides were strongly enhanced in the Atlantic during the LGM, especially in the semi-diurnal band, with tidal energy dissipation (i.e., the loss of energy of the tide to bed friction and to the internal tide) for the M_2 tide a factor 2–3 larger than at present in the open ocean. Changes in the North Atlantic are thought to have been particularly strong with amplitudes tripling with respect to present and exceeding 6 m in the Labrador Sea during the LGM (Griffiths & Peltier, 2008, 2009; Wilmes & Green, 2014). These amplifications resulted from changes in ocean basin shape driven by the $\sim$130 m global mean sea level (GMSL) drop and associated increases in ice sheet extent. Together, these factors rendered the Atlantic more conducive to resonant amplification of the semi-diurnal tides, thus leading to substantial increases in amplitudes and tidal energy dissipation (e.g., Egbert et al., 2004; Green, 2010). Through the deglacial and the

Holocene, energy losses in the deep ocean decreased dramatically whilst the shelf seas (which were emersed during the LGM) re-flooded and became more tidally energetic.

On longer time scales, covering the middle and late Pleistocene ($\sim$770–11.7 ka), sea level fluctuated by 130–145 m as climate cycled between glacial and interglacial phases (e.g., Fox-Kemper et al., 2021). During this period, ice sheet extent followed a saw-tooth shaped pattern: glacial phases were generally characterised by a long-term gradual cooling culminating in a glacial maximum with peak ice sheet extent and sea level lowstands. Subsequently, climate warmed rapidly and transitioned to interglacial conditions, with climate similar to, or warmer than the pre-industrial. GMSL attained highstands of up to $+15$ m and ice sheet extent was similar to, or less than present. The last glacial period spanned from the end of the Last Interglacial (LIG; 130–115 ka; Marine Isotope Stage (MIS) 5e) to the onset of the Holocene, with significant variations in global mean sea level (Waelbroeck et al., 2002; Siddall et al., 2003; Lambeck, 2004; Spratt & Lisiecki, 2016)(see Figure 1a). During the early part of the glacial period (MIS 5 d–a; 115–71 ka), GMSL fluctuated between relative high- and lowstands of -9 and -50 m, respectively (e.g., Creveling et al., 2017). During MIS 4 (71–57 ka), a GMSL lowstand of around -80 m was reached. Thereafter, GMSL rose to a relative highstand during MIS 3 (57–29 ka), though the exact magnitude remains debated (e.g., Dalton et al., 2022). The GMSL lowstand of ~ -130 m during the LGM (MIS 2) was reached between 26.5 and 20 ka (Clark et al., 2009; Lambeck et al., 2014; Peltier et al., 2015; Gowan et al., 2021). At the onset of the deglacial period (19–11.7 ka), GMSL first rose gradually, then more rapidly by around 100 m until the early Holocene ($\sim$8 ka) when present-day levels were reached. Because tides are sensitive to water depth and changes in ocean basin shape and they behave like shallow water waves, it is expected that they are affected by these large sea level changes, as previously seen for the period spanning from the LGM to the present (e.g., Egbert, 2004; Uehara et al., 2006; Green, 2010; Wilmes & Green, 2014; Wilmes et al., 2022; Sulzbach et al., 2023).

In this work, we aim to extend our knowledge of Pleistocene tidal dynamics back to $\sim$430 ka. First, we explicitly model tides over the past glacial cycle covering the period from the LIG to present using two different ice sheet and sea level reconstructions, thus expanding the work in Wilmes et al. (2022) to the entire last glacial cycle. Second, because no spatially and temporally highly resolved global sea level and ice sheet reconstructions exist for the previous multiple glacial cycles, we use the last glacial cycle simulations together with uniform sea level change simulations and extrapolate tidal energy dissipation back to 430 ka based on linear regression analysis. We aim to (1) produce global spatially-varying dissipation estimates for the last glacial cycle which can be used for modelling of the late Pleistocene climate and ocean circulation; and (2) improve our understanding of late Pleistocene tidal dynamics which is relevant for, e.g., SLIPs, ice sheet dynamics, or shelf sea oceanographic processes.

2 Methods

2.1 Tide model

For the tide model simulations, we use the Oregon State Tidal Inversion Software (thereafter OTIS; see Egbert et al., 2004; Green & Nycander, 2013; Wilmes et al., 2019, for details) in its forward mode. OTIS has been used for numerous paleotide (e.g., Egbert et al., 2004; Wilmes & Green, 2014; Green & Huber, 2013; Green et al., 2017) and future tide applications (e.g., Carless et al., 2016; Wilmes et al., 2017; Pickering et al., 2017; Hayden et al., 2020). OTIS solves the linearised shallow water equations (e.g., Hendershott, 1972):

$$\frac{\partial \mathbf{U}}{\partial t} + \mathbf{f} \times \mathbf{U} = -gH\nabla(\zeta - \zeta_{EQ} - \zeta_{SAL}) - \mathbf{F} \tag{1}$$

$$\frac{\partial \zeta}{\partial t} = -\nabla \cdot \mathbf{U} \tag{2}$$

where $\mathbf{U}$ is the depth integrated volume transport, H denotes water depth, $\mathbf{f}$ is the Coriolis vector, g is the gravitational constant, ζ denotes tidal elevation, ζ_{EQ} stands for the equilibrium tidal elevation, and ζ_{SAL} is the tidal elevation due to self-attraction and loading (SAL; i.e., the combined effects of gravitational attraction among the water masses, seafloor deformation, and associated changes in the gravity potential). $\mathbf{F} = \mathbf{F}_B + \mathbf{F}_{IT}$ represents frictional losses due to bed friction ($\mathbf{F}_B$) and tidal conversion ($\mathbf{F}_{IT}$). The former is represented by the standard quadratic law:

$$\mathbf{F}_B = C_d \mathbf{u}|\mathbf{u}| \tag{3}$$

where $C_d = 0.003$ is a drag coefficient, and $\mathbf{u}$ tidal velocity. The energy losses to the internal tide, $\mathbf{F}_{IT} = C_{IT}\mathbf{U}$, depend on a conversion coefficient C_{IT} given by (Zaron & Egbert, 2006; Green & Huber, 2013)

$$C_{IT}(x, y) = \gamma \frac{(\nabla H)^2 N_b \bar{N}}{8\pi\omega} \tag{4}$$

where $\gamma = 37.5$ is a scaling factor (see Zaron & Egbert, 2006, for more details), N_b is the buoyancy frequency at the sea-bed, $\bar{N}$ is the vertical average of the buoyancy frequency, and ω is the frequency of the tidal constituent under evaluation. γ was tuned following the process described in Wilmes and Green (2014) to both minimise present-day amplitude root-mean square errors against TPXO9 and fit TPXO9 dissipation values. Horizontally uniform abyssal stratification was assumed which is parameterized by the buoyancy frequency N through $N(z) = N_0 e^{(-z/1300)}$ with $N_0 = 5.24 \times 10^{-3}$. Sensitivity simulations in Wilmes and Green (2014) and Schmittner et al. (2015), where the sensitivity to glacial interglacial stratification changes was explored, showed that dissipation is rather insensitive to glacial-interglacial stratification changes. Tidal dissipation associated with the combined action of $\mathbf{F}_B$ and $\mathbf{F}_{IT}$ is calculated following the energy balance method outlined in Ray et al. (2003).

2.2 Simulations

2.2.1 Last Glacial Cycle

In our tide model runs, we represent the ice sheet and sea level history over the last glacial cycle with two different ice sheet reconstructions, one external reconstruction by Gowan et al. (2021) and one derived by us, using a global gravitationally self-consistent sea level model. For the latter, we simulate sea level based on the ICE6G_C ice history (Argus et al., 2014; Peltier et al., 2015) that spans the period 122 ka to present with a temporal resolution of 250–500 yrs prior to 21 ka, 1000 yrs up to 32 ka, and 2000 yrs thereafter (referred to as "ICE-6G" from this point onwards. In the sea level model, we compute the time-varying deformation of a rotating, Maxwell viscoelastic Earth model with a depth-dependent Earth structure (e.g., Kendall et al., 2005; Milne & Mitrovica, 1996). For consistency with the global ICE6G_C ice model, we adopt the corresponding VM5a depth-dependent Earth model to represent global Earth structure (Argus et al., 2014; Peltier et al., 2015). Importantly for our application here, the sea level model includes migrating shorelines and the inundation of water into regions previously covered by marine ice (Mitrovica & Milne, 2003). The model formulation is solved using a pseudo-spectral numerical scheme up to spherical harmonic degrees and order 256 (Kendall et al., 2005).

As an alternative to the boundary conditions derived from the ICE6G_C ice sheet history, we use the ice sheet and sea level reconstruction from Gowan et al. (2021). Gowan et al. (2021) presented a global high-resolution ice sheet reconstruction for the period 80 ka to present. The reconstruction is consistent with ice physics but was inferred independently of far-field sea level and δ^{18}O proxy records (i.e., based on ice sheet margins and constructed to be consistent with simple ice sheet physics). The sea level predictions provided by Gowan et al. (2021) also rely on a global gravitationally self-consistent sea level model (SELEN; e.g., Spada & Stocchi, 2007) with a depth-dependent Earth structure, as well as shoreline migration. These reconstuctions have a lower temporal resolution of 2500 yrs.

For our study, both ice sheet reconstructions and the associated sea level change fields were interpolated to the finite-difference grid of OTIS (1/8° spacing in both latitude and longitude) and added to the present-day base topography RTopo-2 (Schaffer et al., 2016). We note that both the ice sheet history and the solid Earth structure, and thus sea level, differ between the two approaches. For the ICE-6G sea levels, tide runs were performed at 2000-year intervals. Each simulation was run with M_2, S_2, K_1 and O_1 equilibrium tidal forcing and a simplified SAL scheme that sets $\zeta_{SAL} = \beta\zeta$, with $\beta = 0.1$. The computational grid extends all the way to 89°N, where it is bounded by an artificial

	RMSE (cm)			Modelled dissipation (TW)			TPXO9 dissipation (TW)		
	deep	shelf	global	deep	shelf	global	deep	shelf	global
M_2	3.7	10.1	4.7	1.2	1.3	2.5	0.8	1.5	2.4
S_2	2.0	4.4	2.3	0.2	0.3	0.5	0.2	0.3	0.5
K_1	1.1	3.2	1.4	0.2	0.2	0.4	0.1	0.2	0.3
O_1	1.2	2.6	1.4	0.1	0.1	0.2	0.1	0.1	0.2

Table 1. Present-day control evaluation. Amplitude root-mean square errors (RMSE) against TPXO9 for the deep ocean (h $>$ 500 m), shelf seas (h $<$ 500 m), and the global ocean. Integrated dissipation values (diss.) are also given for the deep ocean (h $>$ 500 m), shelf seas (h $<$ 500 m), and the global ocean for both the present-day control and for TPXO9.

vertical wall eliminating the need for open boundaries. Although these two simplifications (SAL and pole cap) potentially suppress resonant behavior of the Arctic Ocean during the LGM (Griffiths & Peltier, 2009), the errors incurred in terms of globally integrated dissipation are expected to be small (Sulzbach et al., 2023) and simulations with an iterative SAL scheme carried out previously (Wilmes et al., 2022) show very simlar results for the deglacial.

Additionally, to separate the effect of GMSL changes from land-ocean boundary changes and effects of non-uniform sea level change, we conducted tidal simulations with uniform sea level changes. Here, sea level was uniformly changed from -135 m to $+20$ m in steps of 5 m. Again, RTopo-2 at 1/8° x 1/8° grid spacing was used as the present-day base topography and the simulations were carried out for M_2 and K_1.

The present-day control simulation (i.e., for 0 ka) was benchmarked against the global tidal solution TPXO9-atlas-v5 (`https://www.tpxo.net/global/tpxo9-atlas`) by calculating amplitude root-mean square errors and comparing globally integrated dissipation values; see Table 1. Evidently, the model yields realistic solutions for both diurnal and semi-diurnal tidal constituents.

2.2.2 Multiple glacial cycles (430 ka–present)

Owing to the lack of global bathymetry, ice sheet and sea level reconstructions spanning multiple glacial cycles, it is currently not possible to explicitly model tidal dynamics prior to the LIG. We therefore take a different, novel approach to infer tidal dissipation prior to the last glacial cycle to gain a first-order understanding of tidal dynamics during this period. We first establish regression models between GMSL and globally integrated deep ocean and shelf sea dissipation rates, respectively, using the three simulation sets described above, i.e., runs for (1) the last glacial cycle based on ICE-6G, (2) the last glacial cycle based on Gowan et al. (2021), and (3) uniform GMSL changes. Using the global sea level reconstruction by Spratt and Lisiecki (2016) (thereafter SL16), each regression model is then used to infer tidal dissipation for open ocean and shelf ocean dissipation back to 430 ka. Because GMSL is driven by global ice volume changes, and the ice sheet volume changes over the last multiple glacial cycles generally follow similar patterns (e.g., waxing and waning of the Laurentide and Fennoscandinavian ice sheets) (e.g., Batchelor et al., 2019), we here use GMSL as a proxy for the combined spatially-varying ice volume and sea level changes which drive the changes in the tides. The different bathymetry reconstructions provide a measure of the uncertainty introduced by the differing ice margins.

For the regression models, we chose a polynomial regressions of order two between GMSL (sl) and globally integrated tidal dissipation (D) for the deep and shelf ocean (D_{deep} and D_{shelf}), respectively, for each tidal constituent. The quadratic fit accounts for non-linear interactions between GMSL and dissipation due to e.g., resonance effects. The relationship between GMSL and tidal dissipation thus takes the following form:

$$D_{deep} = \beta_{d0} + \beta_{d1} sl + \beta_{d2} sl^2 \tag{5}$$

$$D_{shelf} = \beta_{s0} + \beta_{s1} sl + \beta_{s2} sl^2 \tag{6}$$

$$D_{total} = D_{deep} + D_{shelf} \tag{7}$$

where $\{\beta_{d0}, \beta_{d1}, \beta_{d2}\}$ and $\{\beta_{s0}, \beta_{s1}, \beta_{s2}\}$ represent the regression coefficients for deep and shelf dissipation for each set of model simulations, respectively. We calculated regression coefficients for the relationships between GMSL and deep and shelf dissipation for all three sets of tide runs, respectively. If the relationship between sl^2 and D was not significant at the 95% confidence level, the order of the polynomial was reduced to one (i.e., linear regression). The relationship between sl and D_{deep} and D_{shelf}, respectively, was calculated separately because, in general, deep and shelf dissipation behaved in an anti-correlated manner in relation to GMSL (i.e., when GMSL decreases, open ocean dissipation increases and shelf dissipation decreases). The globally integrated dissipation D_{total} is given by the sum of D_{deep} and D_{shelf}.

Using each regression model and the SL16 GMSL reconstruction, we then calculated time series of late Pleistocene deep, shelf, and total dissipation. Dissipation values were predicted for each constituent (M_2, S_2, K_1 and O_1) as per Eqs. (5)–(7) and associated standard deviations (σ) were deduced by applying the laws of variance propagation:

$$\sigma^2_{D_{deep}} = \sigma^2_{\beta_{d0}} + \sigma^2_{\beta_{d1}}\ sl^2 + \left(\beta^2_{d1} + (2\beta_{d2} sl)^2\right) \sigma^2_{sl} + \sigma^2_{\beta_{d2}}\ sl^4 \tag{8}$$

$$\sigma^2_{D_{shelf}} = \sigma^2_{\beta_{s0}} + \sigma^2_{\beta_{s1}}\ sl^2 + \left(\beta^2_{s1} + (2\beta_{s2} sl)^2\right) \sigma^2_{sl} + \sigma^2_{\beta_{s2}}\ sl^4 \tag{9}$$

$$\sigma^2_{D_{total}} = \sigma^2_{D_{deep}} + \sigma^2_{D_{shelf}} \tag{10}$$

where sl denotes GMSL from the SL16 reconstruction with the provided formal error σ_{sl}, and $\sigma_{\beta ...}$ denotes the standard deviations associated with the respective regression coefficients.

3 Results

3.1 The last glacial cycle: LIG to present

3.1.1 Ice sheet and sea level evolution

The two ice sheet and sea level reconstructions show pronounced differences during large parts of the last glacial cycle (Fig. 1a and 2). In the following, we will focus on the differences between the two. For a detailed presentation of the two ice sheet and sea level reconstructions, see Gowan et al. (2021), and Argus et al. (2014), Peltier et al. (2015) and Pedersen et al. (in prep). Whilst a fully developed Laurentide Ice Sheet is present from around 100 ka in ICE-6G, a similarly extensive ice sheet is not formed until after 65 ka in the Gowan reconstruction. This leads to a GMSL offset of $\sim$30 m between the two reconstructions during late MIS 5 and early MIS 4 and large differences in shallow shelf sea area. During the MIS 4 peak glaciation, the ICE-6G Laurentide Ice Sheet is slightly more extensive than in Gowan, with the Laurentide Ice Sheet and the Cordilleran Ice Sheet joined up, whereas they remain separated in Gowan. However, the Gowan reconstruction has more extensive ice around Antarctica. Overall, as a result of these differences, ICE-6G sea levels show a slightly lower and earlier MIS 4 GMSL lowstand than Gowan. However, whilst GMSL leading into MIS 4 is similar, there are large regional differences in sea level due to the differences in ice history. The largest differences in ice sheet extent and sea level between the two reconstructions are seen during MIS 3. ICE-6G shows extensive Northern Hemisphere ice sheets throughout MIS 3 whereas in Gowan, ice sheet extent is strongly reduced around 40 ka, with the Fennoscandinavian and Cordilleran Ice Sheets mostly melted and the Laurentide Ice Sheet strongly reduced. These discrepancies lead to an offset in GMSL of around 60 m in the middle of MIS 3 and shelf sea area is approximately doubled in Gowan in comparison to ICE-6G. Towards the LGM, both reconstructions show expanding ice sheets and a drop in GMSL. ICE-6G shows slightly more extensive Northern Hemisphere ice sheets, whereas Gowan shows a stronger expansion of the Antarctic ice sheet margins. The ICE-6G sea level lowstand occurs around 26 ka, whereas, for Gowan, it does not take place until 20 ka, and is around 20 m less than for ICE-6G. From 20 ka to present, both simulations show a similar GMSL evolution. However, again, there are pronounced differences in regional sea levels (locally, > 50 m offsets) due to differences in instantaneous ice sheet loading but also ice history.

3.1.2 Amplitude evolution

Large changes in tidal amplitudes (regionally in excess of 4 m) occur over the last glacial cycle for both sea level reconstructions, but, owing to the discrepancies in sea level and ice sheet history, there are pronounced offsets between the tidal histories (see Figs. 3 and 4 for total amplitude changes). In the following, we discuss how each constituent contributes to the total amplitude changes, focusing the description on the areas that show the largest changes and laying the emphasis on M_2, which shows the largest absolute changes.

For the ICE-6G simulations, M_2 amplitudes (Figure S1 in Supporting Information S1) show levels similar to present-day during the LIG. But, M_2 amplitudes in the North Atlantic, in the Weddell Sea and to a lesser extent in the South Atlantic and in the Gulf of Panama rapidly increase at the termination of the LIG and onwards. A further increase in amplitudes in these areas occurs from 68 ka onward towards the sea level lowstand around 60 ka, where, additionally, the Arctic shows large tidal amplitudes (> 3 m in the Chukchi Sea). After 60 ka, the enhancements persist, albeit at a slightly reduced level. During the transition to the LGM, North Atlantic amplitudes increase further to peak round 20 ka, however, Weddell Sea amplitudes are much reduced in comparison to MIS 3 because of the more extensive grounded ice in the bay. During the deglacial, pronounced drops in North Atlantic and Arctic M_2 amplitudes take place, and by 8 ka tidal amplitude reach near-present day levels.

For the Gowan simulations, M_2 amplitudes (Figure S5 in Supporting Information S1) between 80 ka and 72.5 ka show similar levels to present, apart from considerably larger amplitudes in the Weddell and Ross Sea area. As the sea level lowstand around 60 ka is approached, North Atlantic amplitudes strongly increase. These enhancements persist (albeit at a smaller magnitude) until $\sim$55 ka, after which the North Atlantic oscillates between periods of larger and smaller M_2 amplitudes with peaks around 45 ka, 37.5 ka and 32.5 ka. Notable are also strongly increased tides in the Ross Sea between 50 and 40 ka. Large North Atlantic amplitudes develop towards the LGM and during the early to mid deglacial (peaking around 17.5 ka and persisting until 12.5 ka). During LGM, strong enhancements in Arctic tides can also be seen.

For the ICE-6G runs, S_2 amplitudes (Figure S2 in Supporting Information S1) are similar to present at the end of the LIG. During the early glacial, Labrador Sea and North Atlantic amplitudes increase, but the increases are less pronounced than for M_2. Furthermore, large S_2 amplitudes occur in the Coral Sea (NE Australia). The two sea level lowstands ($\sim$60 ka and LGM) are characterised by large North Atlantic tides and strong enhancements in Arctic S_2 amplitudes. S_2 amplitudes in the Gowan simulations (Figure S6 in Supporting Information S1) follow a similar picture as M_2 amplitudes albeit with a lower magnitude. Notable is that Arctic S_2 amplitudes enhancements are much reduced in the Gowan simulations and are only present during the middle of the LGM.

In the ICE-6G runs, K_1 and O_1 tidal changes (Figure S4 in Supporting Information S1) are mainly regional. During the sea level lowstands around 62 ka and during the LGM, Pacific shelf seas (Sea of Okhotsk, South China Sea and Banda Sea) become resonant. During the remainder of the last glacial cycle, amplitudes remain close to their present-day levels.

Similarly, both K_1 and O_1 amplitudes are characterised by mainly regional changes in the Gowan simulations (Figures S7 and S8 in Supporting Information S1). During periods of sea level lowstands ($\sim$62.5–55 ka and 27.5–15 ka), increased amplitudes can be see around Antarctica and in the shelf seas of the Pacific, whereas other parts of the ocean seem rather insensitive to the large sea level and ocean basin shape changes.

3.1.3 Dissipation evolution

For M_2, global open ocean dissipation in the ICE-6G simulation is at near-present-day values during the LIG (Figure 1b). It approximately doubles over a period of $\sim$10 kyr between 120 and 110 ka to $\sim$2 TW when N and S Atlantic dissipation increases (see Fig. 5). It remains elevated at this level until around 70 ka when dissipation rises by a further 25% (0.5 TW) driven by Arctic and N and S Atlantic dissipation increases. Open ocean dissipation remains at these elevated values peaking around 65 ka, 40 ka and during the LGM, with only a small dip occurring around 28 ka. From 68 ka to 30 ka, open ocean dissipation in the Southern Ocean more than doubled in the ICE-6G runs driven by increases in the Weddell Sea area which increases Southern Hemisphere dissipation to levels greater than in the Northern Hemisphere (Figure S9 in Supplementary Information S1). During MIS 4 to MIS 2, dissipation increases around the European Shelf, in the Labrador Sea, Denmark Strait, Norwegian Sea, along the mid-Atlantic ridge, in the Arctic Basin and also in the South Atlantic. In contrast, the Gowan simulations show near present-day open ocean dissipation values (apart from around Antarctica which increases Southern Hemisphere dissipation; Figure S9 in Supplementary Information S1) prior to the sea level lowstand around 60 ka when they increase by $\sim$50% during the sea level lowstand through Atlantic enhancements (see Fig. 6). Thereafter, dissipation decreases slightly, but oscillates through three distinct troughs and peaks. It is notable that Hudson Bay & Strait dissipation is significantly anti-correlated with North Atlantic dissipation, suggesting that when Hudson Bay & Strait lies dry or is ice covered, North Atlantic dissipation peaks. Towards the LGM, dissipation increases again, and reaches its peak during the early deglacial phase with a 90% increase relative to present driven by increases in Atlantic (especially North Atlantic) and Arctic dissipation, whereas in the ICE-6G simulations, dissipation in the Southern Hemisphere decreases—in contrast to the Gowan simulations.

Despite the large differences in shelf area (see Fig. 1a), the evolution of shelf sea dissipation is relatively similar between the two sets of simulations. Between 120 and 70 ka, shelf dissipation is at levels similar to present. With the decrease in sea level towards the lowstand around 60 ka, shelf dissipation decreases by $\sim$40% and remains reduced until the onset of the Holocene with values halved with respect to present during the LGM. In the Gowan simulation, around 40 ka, the values increase to present-day levels and then decrease again to their LGM minimum. Overall, for M_2, the simulations suggest that open ocean dissipation was enhanced for most of the last glacial period, but that the exact magnitude is dependent on the sea level and ice sheet evolution. Less M_2 energy was lost in the shelf seas between 70 ka and the onset of the Holocene and more M_2 energy dissipated in the open ocean. Overall, the results from the ICE-6G simulations suggest that total dissipation was larger than present for most of the glacial cycle, on average 25% (maximum $\sim$40%), whereas for the Gowan simulations which only extend back to 80 ka, the average increase was only 7% (maximum 28%).

For S_2 (Figure 1c), in contrast, total dissipation is lower than present for most of the glacial cycle, except for the Holocene (for ICE-6G, the average decrease is 15%). This is driven by pronounced decreases in shelf sea dissipation which are strongest between 70 ka and the mid-deglacial. The magnitude of the decrease (up to 60% with respect to present) is slightly larger in the ICE-6G simulations due to the larger reduction in shelf area. Deep dissipation is slightly elevated (20–30%) in the ICE-6G simulation, but reduced with respect to present (apart from the LGM period) in the Gowan simulation.

For K_1 (Figure 1d), the overall pattern is similar to S_2, with total dissipation being slightly reduced for most of the glacial cycle (for ICE-6G by $\sim$10%) driven by lower levels of shelf sea dissipation. Again, open ocean dissipation in the ICE-6G simulation is enhanced between 70 ka and the onset of the Holocene and shelf sea dissipation remains reduced; whereas in the Gowan simulation, there are two distinct peaks situated around the sea level lowstands at 60 ka and the LGM. Between the lowstands, open ocean dissipation and shelf sea dissipation returns to present-day values.

For O_1 (Figure 1e), the shelf sea dissipation signal is similar to S_2 and K_1, but the decreases are compensated by increases in open ocean dissipation, such that total dissipation remains at values near present for most of the glacial cycle and an increase of up to 38% in total dissipation occurs during the peak of the LGM (cf. Sulzbach et al., 2023).

Overall, this means that, for the Gowan simulations, globally integrated dissipation, on average, was close to present-day levels between 80 ka and present, but for the ICE-6G simulations, total dissipation over the whole glacial cycle was on average $\sim$15% larger than at present (Figure 1f). Deep dissipation in the ICE-6G runs was 57% greater on average (80% larger between 66 ka and 16 ka), and raised by 34% in the Gowan simulation. For shelf dissipation the mean reductions for ICE-6G and Gowan are 22 and 24%, respectively.

3.2 Tidal evolution over the last 430 kyr

3.2.1 Relationship between GMSL and tidal dissipation

For the ICE-6G simulations, open ocean dissipation is highly and significantly anti-correlated with GMSL for all constituents ($r < -0.88$ for all constituents)—i.e., when sea level drops, open ocean dissipation increases (see Fig 7). For shelf dissipation, similarly high magnitude significantly positive correlations emerge ($r > 0.95$) but the relationship is opposite, i.e., decreasing sea levels reduce shelf dissipation. In contrast, total dissipation shows a weaker albeit still significant relationship with GMSL, owing to the opposing relationships of open ocean and shelf dissipation. For M_2 and O_1, total dissipation is anti-correlated with GMSL (i.e., larger dissipation with lower GMSL), whereas for S_2 and K_1 we observe the reverse. For the Gowan simulations, correlations generally have the same sign as the correlations in the ICE-6G simulations, but with slightly reduced magnitudes. Dissipation from the uniform sea level drop simulations shows similarly high negative correlations between GMSL and open ocean dissipation as the ICE-6G simulations, and highly positive correlations between GMSL and shelf dissipation.

Next, we evaluate the polynomial regression fit between GMSL and both shelf and open ocean dissipation for each tidal constituent for all three sets of simulations, respectively (see Fig. 8). For open ocean dissipation, all constituents apart from S_2 show $r > 0.95$ between actual and estimated dissipation values, and for shelf dissipation all regression models can explain more than 89% of the variability. For the Gowan simulations, the regression fit is good for the diurnal constituents but shows a slightly less good fit for the semi-diurnal constituents ($r = 0.65$ and $r = 0.68$ for M_2 and S_2, respectively). Regression-based total dissipation for each constituent (Figure S10 in Supplementary Information S1), calculated as the sum of D_{deep} and D_{shelf} from the regression models for each constituent, compares well with explicitly modelled dissipation ($r > 0.90$) for ICE-6G. A similarly good fit can be achieved with the uniform SL simulations. However, it is notable that for M_2, the uniform SL simulations show only very small variations in dissipation (< 0.2 TW for GMSL variations between -135 m to $+20$ m) in comparison to the ICE-6G simulations (> 1.1 TW for GMSL variations between -130 m and $+3$ m), as increases in open ocean dissipation increases are balanced by decreases in shelf dissipation. For the Gowan simulations, the regression models are able to reproduce explicitly modelled values for all constituents well, apart from M_2, where the regression model produces near constant total dissipation values and correlation between explicitly and regression total modelled dissipation is not significant.

Interestingly, pronounced differences emerge in the relationship between GMSL and M_2 open ocean dissipation (Fig. 8) across the sets of simulations. Whilst both ICE-6G and the uniform SL simulations show a strongly negative relationship, the slope of the relationship is very different, with the uniform SL simulations showing much smaller increases in dissipation than the ICE-6G simulations for the equivalent GMSL decrease. The Gowan simulations fall somewhat between the two other estimates. These differences may reflect the strong control exerted by coastline positions on the large M_2 open ocean tides (e.g., Arbic et al., 2009; Green, 2010; Wilmes et al., 2019), especially as differences in ice sheet extent and non-uniform sea level changes cause offsets in coastlines in comparison to the uniform sea level drop case. On the other hand, the non-uniform sea level changes driven by GIA processes, which are especially pronounced close to ice sheets where we generally see the largest tides, may also be contributing to these differences (see, e.g., Arbic et al., 2008).

3.2.2 Dissipation estimates over the last 430 kyr

Following on, we now use the SL16 sea level curve and associated errors (Fig. 9a) to infer dissipation back to 430 ka by applying all three regression models. The SL16 sea level curve shows large variability in GMSL with sea level fluctuating between highstands of ~ -8 m and $+16$ m during the interglacials and sea level lowstands of 98–129 m during glacial maxima. On average, GMSL was 54 m lower than present over the last 431 ka, according to SL16. The SL16 GMSL estimate compares well with the ICE-6G derived GMSL for the last glacial cycle ($r = 0.98$, $p = 0.00$) (Fig. 9a). Small offsets (∼15 m) can be seen during MIS 5, when climate entered into the last glacial phase. However, large differences emerge between SL16 and Gowan, which are especially pronounced during MIS 3 and late MIS 5.

Regression-inferred dissipation values for the last glacial cycle closely follow the explicitly modelled values both for ICE-6G and Gowan (Fig. 9b–k). The largest offsets occur when the sea level curves of ICE-6G and Gowan disagree with SL16, e.g., around the relative sea level highstands at 100 ka and 80 ka for ICE-6G, and during MIS 3 for Gowan. The disparities are most pronounced for M_2 open ocean dissipation. Looking back over the last four glacial cycles, the ICE-6G regression model suggests that M_2 open ocean dissipation was strongly increased with respect to to present—on average by 120%, i.e., more than doubled—apart from during interglacial phases. When GMSL drops by more than 100 m, M_2 open dissipation increases on average by a factor 2.6. For the Gowan model, the mean M_2 open ocean enhancements (36%) are less pronounced and and open ocean dissipation during sea level lowstands increased by a factor 1.7. These Gowan change estimates are very similar to those obtained using the uniform SL model (Figure S11 in Supplementary Information S1). For shelf dissipation, all three models give very similar results, estimating the mean decrease in dissipation to be around 20% over the last 430 kyr. Total M_2 dissipation averaged over the last 430 kyr was between 3% (uniform SL), 5% (Gowan) and 37% (ICE-6G) greater than at present. For the other constituents, average total dissipation changes are less pronounced, generally within $\pm 25\%$. However, considerable fluctuations in the partitioning of tidal energy between the open ocean and the shelf seas can be seen; with S_2, K_1 and O_1 open ocean dissipation increasing during glacial periods and decreasing towards present-day values during interglacials, respectively, and shelf dissipation behaving in an opposing manner. Taken together, these results suggest that globally integrated open ocean dissipation was on average between 28 % (Gowan) and 85 % (ICE-6G) greater than at present, with enhancements by a factor 1.5 to 2.2 during sea level lowstands and values similar to present during highstands. However, it is worth noting that the exact magnitude of the estimated changes is dependent on the specific sea level (and ice sheet) model adopted.

4 Discussion and Implications

Our simulations are able to reproduce the findings of other studies for the LGM, deglacial and Holocene (Arbic et al., 2004; Uehara et al., 2006; Griffiths & Peltier, 2008, 2009; Green, 2010; Wilmes & Green, 2014; Wilmes et al., 2019, 2022), but also provide the first continuous estimates of tides and tidal dissipation for the last 430 kyr, thus expanding our knowledge on tidal dynamics prior to the LGM.

Our results show that, apart from interglacial phases, tides and tidal dissipation were different from present during most of this extended time period, covering multiple glacial-interglacial cycles. Changes were especially pronounced for the M_2 tidal constituent, which displays near-resonant behaviour during the LGM (Arbic et al., 2004; Uehara et al., 2006; Griffiths & Peltier, 2008, 2009; Green, 2010; Wilmes & Green, 2014; Wilmes et al., 2019). Our results show that the M_2 tide in the open ocean was strongly enhanced with respect to present for most of the last glacial cycles, whereas for the constituents S_2, K_1 and O_1 the relative enhancements were smaller and confined to periods with the lowest sea levels. Peak open ocean amplitudes and dissipation occurred when GMSL dropped below 70 m. Notably, for the LGM and for both the ICE-6G and Gowan simulations, peak dissipation values do not coincide with the lowest sea levels and greatest ice sheet extent but reach their maximum 4–5 kyr after the lowstand as the ice begins to recede and sea level begins to increase (at 22 ka for ICE-6G and 15 ka for Gowan). This is likely related to the location of grounded ice margins and thus regional shelf area which in turn affects resonance properties of the glacial Atlantic (see experiments in Wilmes et al., 2019, which show that reduced Weddell Sea ice extent increases Atlantic dissipation by $\sim$1 TW).

However, there are considerable differences between the two reconstructions for the last glacial cycle, and thus differences in the simulated tides. Whilst the two reconstructions show relatively similar GMSL and ice sheet extent from 20 ka to present and agree during the two peak glaciations (LGM and MIS 4), they strongly differ in ice sheet extent and GMSL during MIS 3 (55 ka to 25 ka) and late MIS 5 (80 ka to 65 ka) (see Fig. 2). The ICE-6G reconstruction shows an extensive Laurentide ice sheet (LIS) from 80 ka and Fennoscandia is largely covered by ice from 70 ka onwards. In contrast, the Gowan reconstruction has extensive ice sheets over North America and Fennoscandia only during the glacial periods around 60 ka and the LGM. Ice sheet extent leading up to these periods (80–65 ka and 55–30 ka) is much reduced in comparison to ICE-6G, and restricted to smaller more localised ice caps (see Fig. 2). This leads to pronounced differences in local relative sea level of over 100 m and GMSL offsets of over 65 m between the two reconstructions during MIS 3 (see Figure 1a and Fig. 2). GMSL during MIS 3 is subject to high uncertainty with sea level estimates for this periods remaining debated (e.g., Pico et al., 2016, 2017; Dalton et al., 2016, 2022). Because of a lack of direct markers of GMSL prior to the LGM, pre-LGM GMSL is often inferred from proxy records such as δ^{18}O from benthic foraminifera (e.g., Waelbroeck et al., 2002) or planktonic foraminifera (Shakun et al., 2015), from spleotherms in the Red Sea (Grant et al., 2014; Rohling et al., 2009) and compilations from multiple statistically analysed records (Spratt & Lisiecki, 2016). However, because δ^{18}O carries the imprint of both global ice-volume and ocean-temperature changes, the records need to be corrected for temperature changes to obtain sea level curves (e.g., De Boer et al., 2014). Large offsets in MIS 3 GMSL of 30–60 m have been found between ice sheet based reconstructions (e.g., Pico et al., 2016, 2017; Dalton et al., 2016; Gowan et al., 2021; Dalton et al., 2022) and records inferred from marine δ^{18}O (e.g., Waelbroeck et al., 2002; Spratt & Lisiecki, 2016), with ice sheet reconstructions suggesting that (i) the Laurentide Ice Sheet during MIS 3 was much less extensive than previously thought and (ii) GMSL was $\sim$30–50 m lower than at present (Pico et al., 2016, 2017; Dalton et al., 2016, 2022). This implies that, for MIS 3, the Gowan sea level and ice sheet reconstruction may be more appropriate as it captures the relative sea level highstand and reduced ice sheet extent.

By comparing the ICE-6G and Gowan tide simulations for the LGM, it becomes apparent how sensitive the tidal dynamics are to relative small changes in bathymetry, i.e., changes in both sea level and ocean basin shape (e.g., through ice sheet extent changes) when in a near-resonant state. At 20 ka, M_2 open ocean dissipation differs by 0.5 TW between the ICE-6G and Gowan simulation, despite a very similar GMSL drop of 116 m and 120 m, respectively. Experiments in Wilmes et al. (2019) showed that LGM M_2 tidal dynamics were remarkably insensitive to offsets in GMSL ($\pm$10 m) but that changes in the location of the land-ocean boundaries could have dramatic effects (e.g., altering ice sheet extent in the Weddell Sea led to a $>$ 1 TW change in M_2 dissipation). This is also shown when comparing the uniform SL change simulations with those that have realistic glacial land ocean boundaries (1.8 TW versus 2.5 and 2.0 TW for ICE-6G and Gowan, respectively). Comparing the ICE-6G and Gowan 20 ka bathymetries (see Fig. 2) shows that the Gowan reconstruction has more ice around the margins of the Laurentide and the Greenland Ice Sheets but also around the margins of Antarctica. Furthermore, whilst GMSL is very similar between the two reconstructions, regional sea levels in the Labrador Sea differ by over 50 m (Fig. 2) which may also influence tidal dynamics and contribute to the dissipation offsets. It is also worth noting that the LGM sea level lowstand does not occur at the same time in the two reconstructions: in ICE-6G, the lowest sea levels occur around 26 ka, whereas for Gowan they occur at 20 ka, and the ICE-6G lowstand is 10 m lower than in Gowan (-130 m versus -120 m).

This work and that of Wilmes et al. (2019) demonstrate that small changes in land-ocean boundaries, e.g., through changes in ice sheet extent, could dramatically alter open ocean tidal energy dissipation on the order of $\pm$1 TW. In experiments using the intermediate climate model UVic (Schmittner et al., 2015; Wilmes et al., 2019, 2021), changes of this order of magnitude correspond to a $\sim$2–4 Sv change in AMOC strength. These strong sensitivities in glacial tides could cause rapid changes in the amount of tidal energy available for ocean mixing which, in turn, could impact ocean circulation and thus climate. Feedbacks between tides, ice sheet extent, ocean mixing, and climate may be a modulating factor for glacial climate, especially for period such as Heinrich events, where ice loss from Hudson Strait has been postulated to have affected tidal dynamics and vice versa (e.g., Arbic et al., 2004; Velay-Vitow et al., 2020). For instance, in the Gowan simulations, between 60 ka and 25 ka, fluctuations in M_2 open ocean dissipation can be seen which appear related to Hudson Bay & Strait dissipation, thus suggesting that Hudson Bay & Strait ice cover may affect (North) Atlantic tidal energy availability. Furthermore, the large tides along the ice sheet margins—both for the Antarctic and Northern Hemisphere ice sheets—may have contributed to the rapid ice sheet retreat linked with the deglacial increase in sea level (Gomez et al., 2020; Batchelor et al., 2023), for example, through ice shelf tidal flexure and crevasse formation (e.g., Olinger et al., 2019).

Because the sea level simulations used for the last glacial cycle include no ice history prior to 122 ka (ICE-6G) and 80 ka (Gowan), the oldest timeslices (i.e., LIG for ICE-6G and late MIS 5 for Gowan) are likely associated with the largest errors, as each time step is affected by previous ice sheet and sea level history. For example, because no ice history was present for the penultimate glacial maximum, the exact sea levels and thus tides during the LIG, are likely subject to larger errors. It is also possible that, due to ice history 'memory' from previous glaciations, tidal dynamics moving into a glaciation may behave differently than during the deglacial phase. However, at present, due to a lack of global high resolution ice sheet reconstructions beyond the LIG, it is not possible to evaluate this point. Another source of uncertainty is the relatively low temporal resolution of the ice sheet histories (2.5 kyr for Gowan throughout the last glacial cycle and 2 kyr prior to 32 ka for ICE-6G, $\leq$ 1 kyr after 32 ka) and for ICE-6G, the horizontal resolution of the ice sheets ($1/2° \times 1/2°$). It is conceivable that the adopted histories lack small scale ice sheet and bathymetry fluctuations, which, during tidally resonant states, could have led to large short-term regional and supraregional shifts in tidal dynamics.

Simulations of climate during the last glacial cycle or parts thereof generally neglect transient changes in tidal energy input to ocean mixing and hold mixing rates constant at the present-day or glacial state (e.g., Menviel et al., 2017; Pöppelmeier et al., 2023). However, this work emphasises that tidal dissipation strongly varied between glacial and interglacial phases and that large short-term variations may have occurred during transitions into and out of glacial phases. The explicitly simulated glacial cycle tidal dissipation timeslices can be used to adjust vertical mixing in transient climate model simulations. These also account for regional responses in dissipation which may differ from the global mean (e.g., during MIS 3 dissipation dissipation enhancements in the Southern Hemisphere are greater than in the Northern Hemisphere which stands in contrast to full glacial conditions during the LGM).

5 Conclusion

In this study, we have simulated tidal amplitudes and tidal dissipation for the last glacial cycle encompassing the LIG to present. In addition, we have estimated tidal dissipation for the last four glacial cycles spanning back to 430 ka. Our findings suggest that tides likely differed from present during most glacial phases, with maximum tidal amplitudes and open ocean dissipation occurring during sea level lowstands due to the resonant properties of the glacial ocean with regards to the semi-diurnal tidal forcing. Additionally, we discovered that during glacial phases, semi-diurnal tides, particularly M_2, were highly sensitive to sea level and ice sheet extent, which remain uncertain prior to the LGM. These results are of wider relevance as they indicate that the availability of tidal energy during the late Pleistocene strongly differed from the present, potentially impacting ocean mixing, and thus ocean circulation and climate in the past.

6 Open Research

The data used in this study are available using the following links: Gowan et al. (2021) ice sheet and sea level reconstruction `https://doi.pangaea.de/10.1594/PANGAEA.905800`, ICE-6G ice sheet reconstruction https://www.atmosp.physics.utoronto.ca/~peltier/data.php, TPXO9 tidal atlas https://www.tpxo.net/global/tpxo9-atlas and RTopo-2 https://doi.pangaea.de/10.1594/PANGAEA.856844. The tidal simulations and relevant grid files together with the Matlab routines necessary to read the data are available at the repository Zenodo via doi:10.5281/zenodo.8147509 (https://zenodo.org/record/8147509) with open access (Wilmes et al., 2023).

Acknowledgments

SBW and JAMG were funded through NERC grant NE/S009566/1. MS was supported by the German Research Foundation (DFG, Project no. 451039647). Simulations were done on Supercomputing Wales through Bangor University.

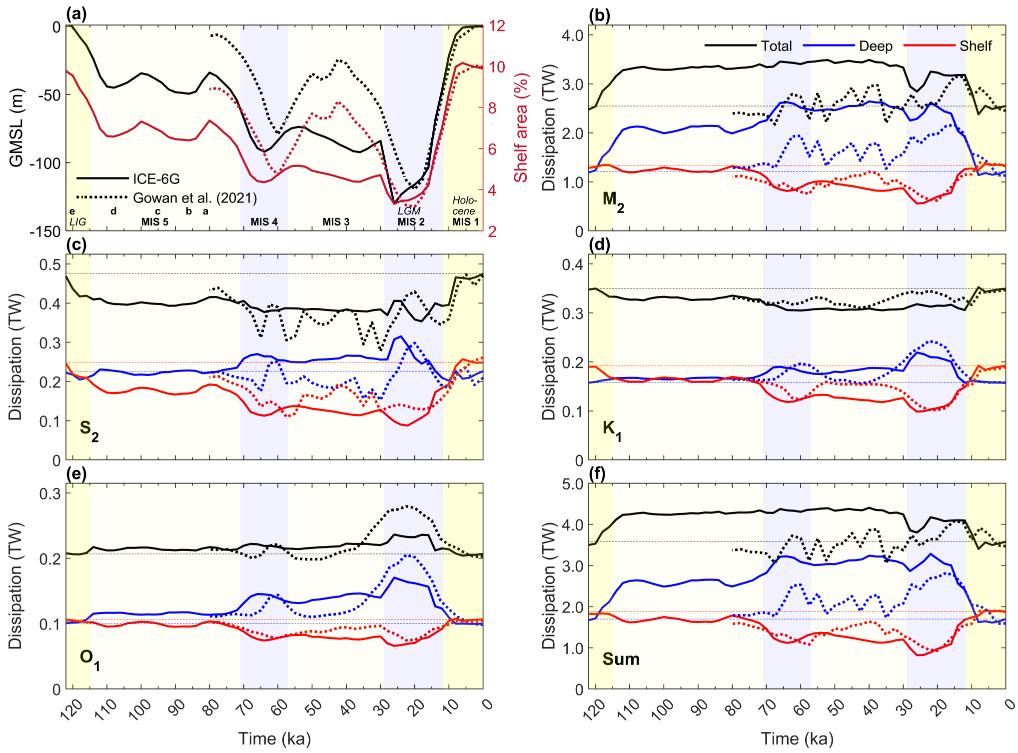

Figure 1. (a) Global mean sea level (black line) and shelf area (in % of global ocean area) for ICE-6G (solid lines) and Gowan (2021) (dotted lines). Marine isotope stages 1 to 5 are indicated by shading and labels above the timeline. For MIS 5, letters indicate substages. Interglacial periods are highlighted by yellow shading. Italic labels show climate periods: LIG = Last Interglacial; LGM = Last Glacial Maximum. (b–e) Dissipation for the constituents M_2, S_2, K_1 and O_1, respectively. Open ocean (deep) dissipation is plotted in blue, shelf sea dissipation in red and globally integrated dissipation in black. ICE-6G values are plotted with solid lines and Gowan (2021) values with dashed lines. (f) same as (b–e) but for the sum of the constituents. The dashed thin straight lines give present-day values as a reference.

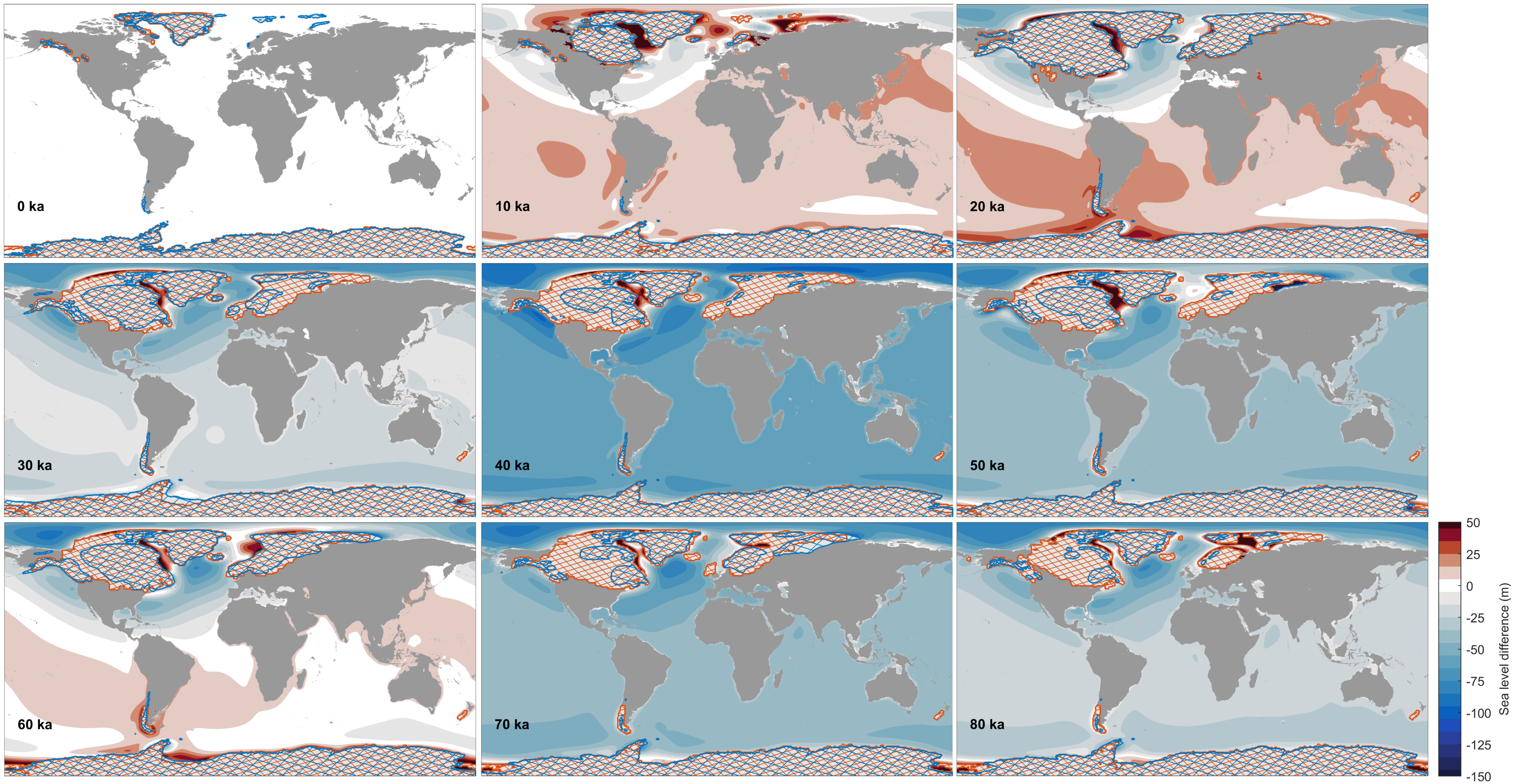

Figure 2. Differences in sea level and ice sheet extent between ICE-6G bathymetries and Gowan et al. (2021) for selected timeslices. Differences in sea level change plotted as ICE-6G minus Gowan (i.e., blue colours indicate lower sea levels in ICE-6G and red colours higher sea levels in ICE-6G than in Gowan). ICE-6G ice sheet extent is indicated with orange hashing, Gowan ice sheet extent is given with blue hashing.

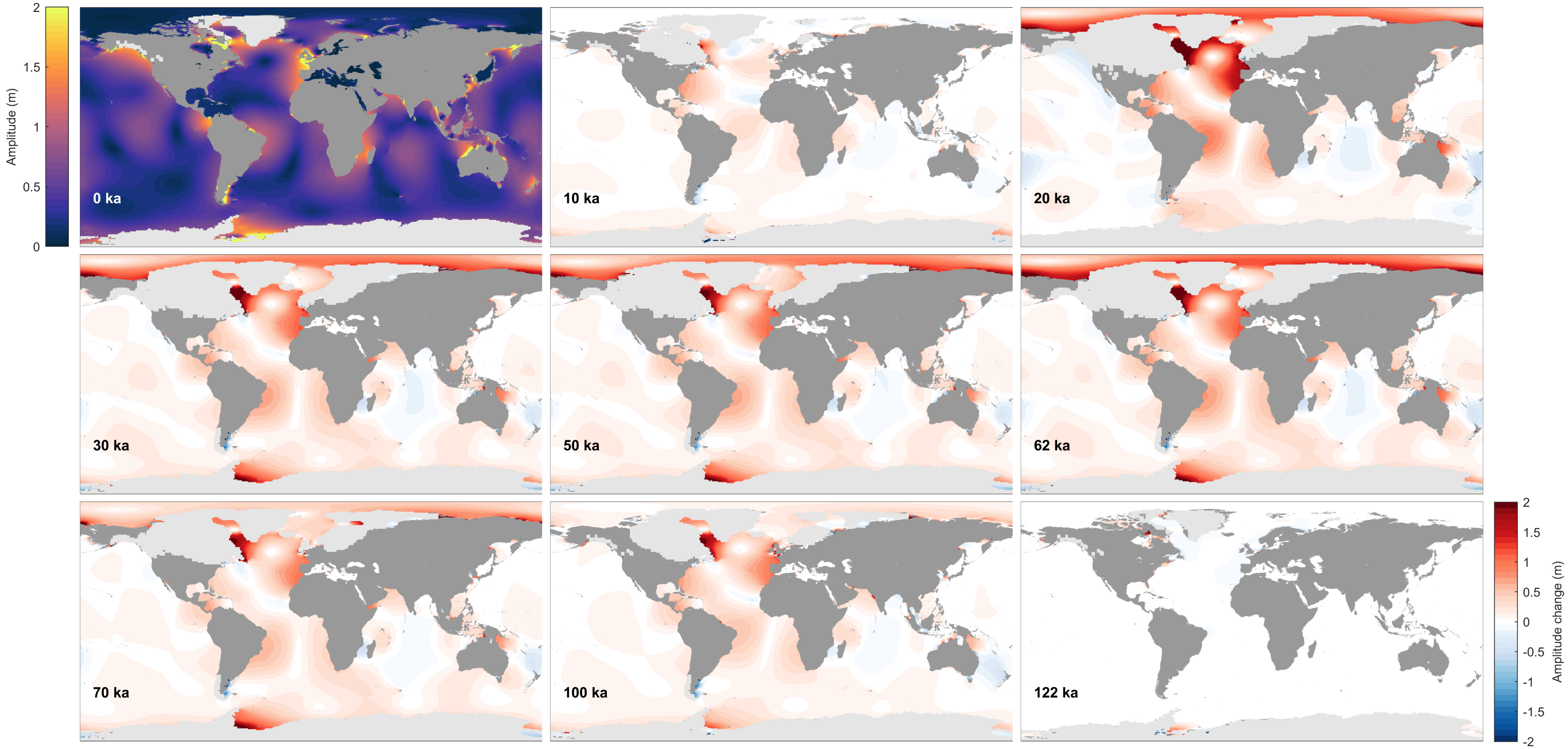

Figure 3. (top left) Present-day tidal amplitudes plotted as the square-root of the sum of the squared amplitudes ($\sim$ equivalent to mean high water levels) of the constituents M_2, S_2, K_1 and O_1. (remaining panels) Tidal amplitude (shown as the square-root of the sum of the squared amplitudes of the constituents M_2, S_2, K_1 and O_1) changes with respect to present for selected time slices over the last glacial cycle for the ICE-6G simulations. Land is shaded in dark grey and land ice coverage is indicated in light grey.

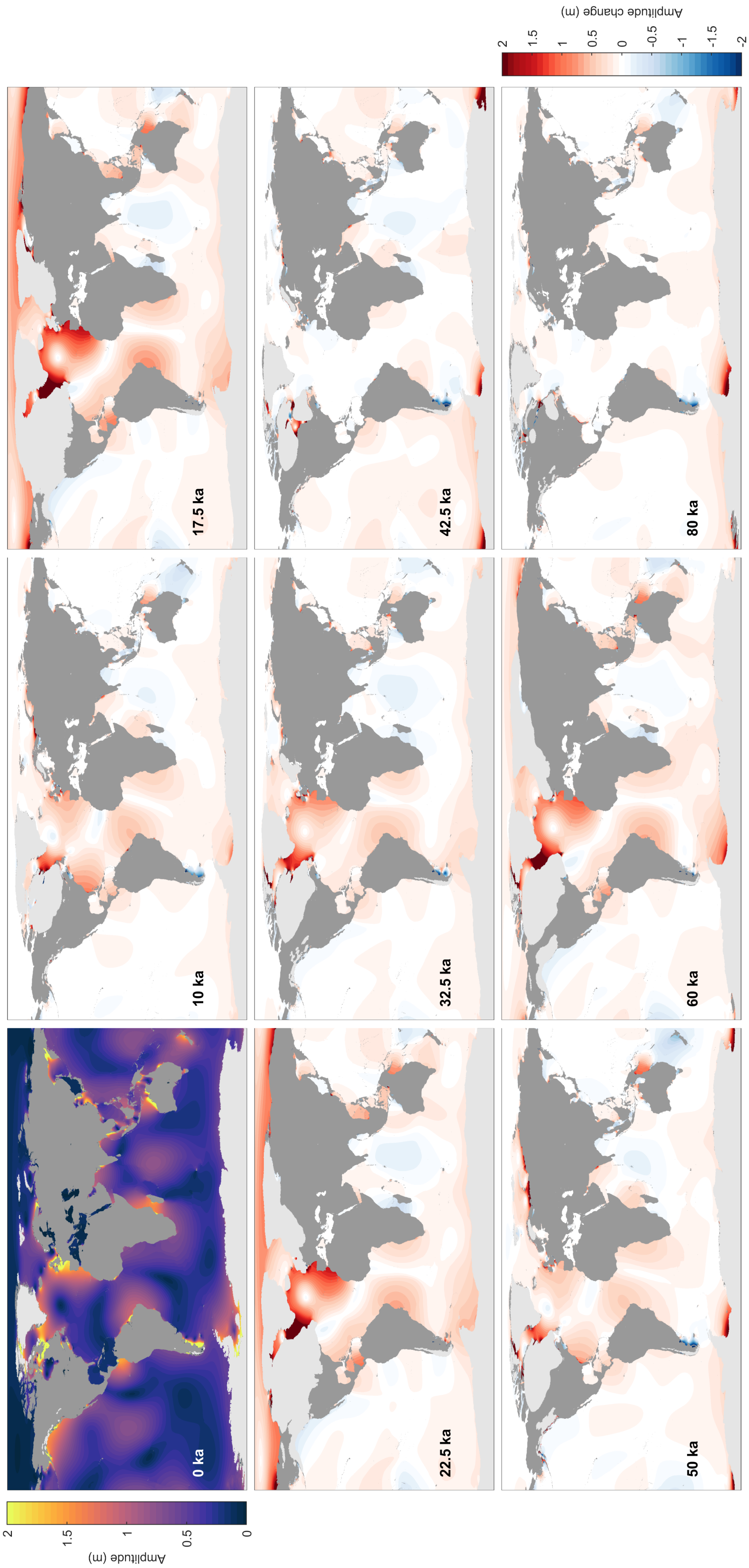

Figure 4. Same as Figure 3 but for the Gowan simulations

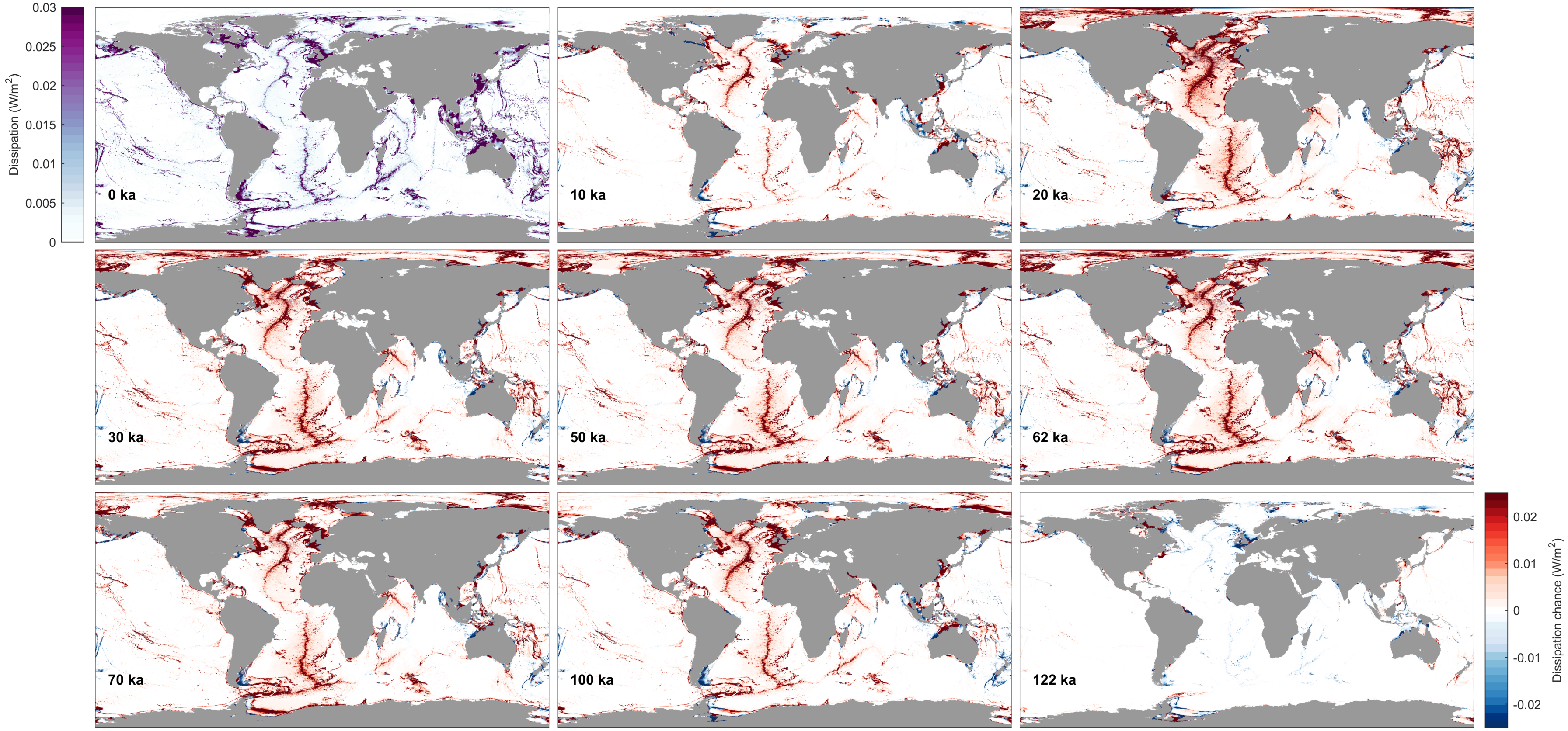

Figure 5. (top left panel) Present-day tidal dissipation plotted as the sum of the dissipation of the constituents M_2, S_2, K_1 and O_1. (other panels) Dissipation (as sum of constituents M_2, S_2, K_1 and O_1) difference with respect to present for selected time slices over the last glacial cycle for the ICE-6G simulations. Land is shaded in grey.

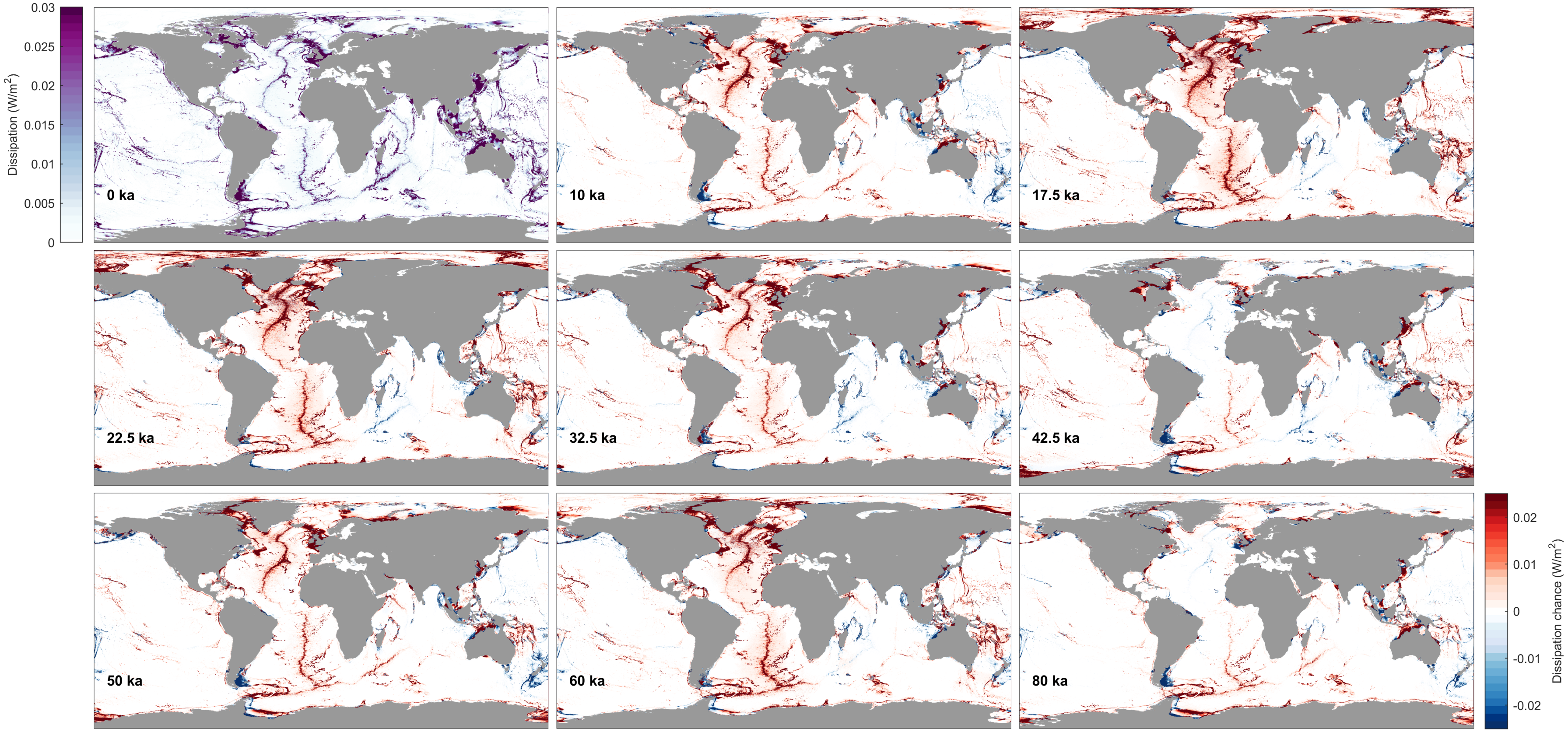

Figure 6. (top left) Present-day tidal dissipation plotted as the sum of the dissipation of the constituents M_2, S_2, K_1 and O_1. (other panels) Dissipation (as sum of constituents M_2, S_2, K_1 and O_1) difference with respect to present for selected time slices over the last glacial cycle for the Gowan simulations. Land is shaded in grey.

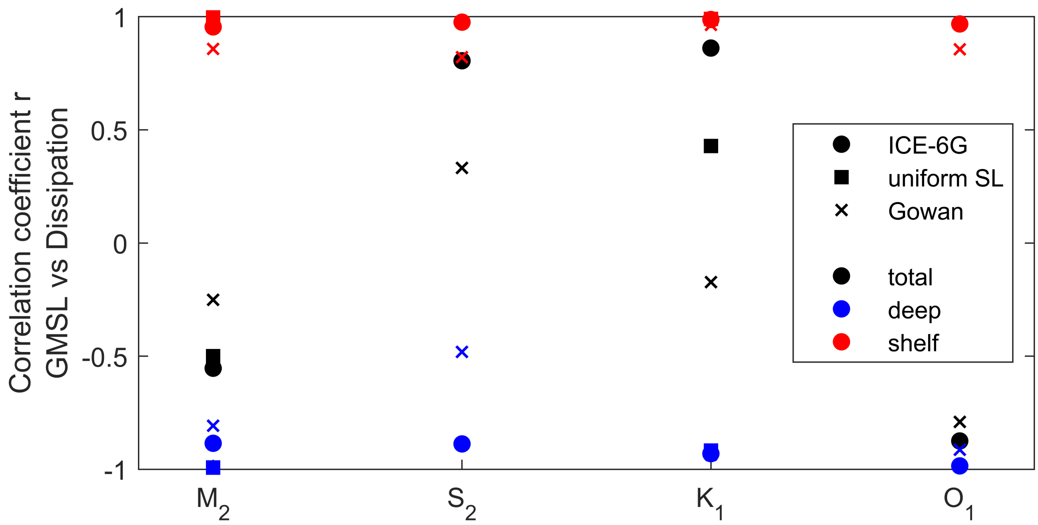

Figure 7. Correlation coefficients between GMSL and dissipation by tidal constituent from runs with ICE-6G bathymetry (circular markers), with uniform sea level changes (squares) and the Gowan bathymetries (crosses). Blue markers are used for open ocean dissipation, red ones for shelf sea dissipation and black ones for globally integrated dissipation.

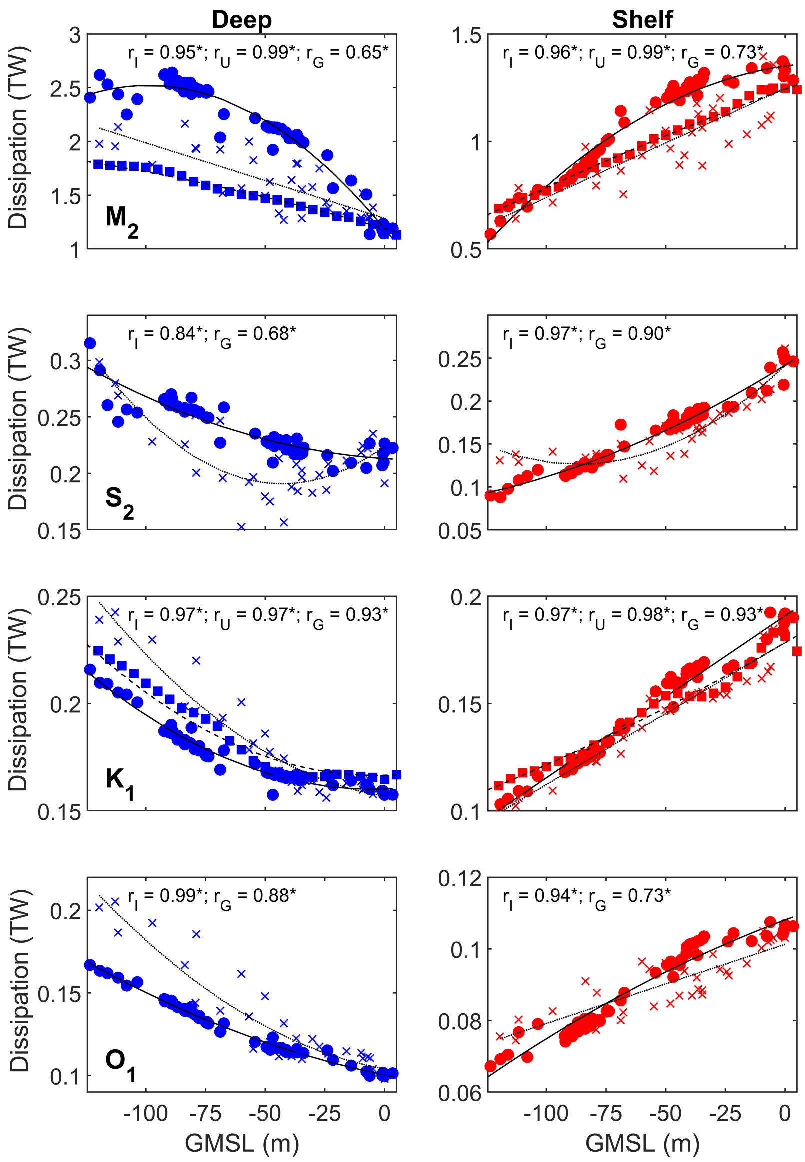

Figure 8. Open ocean dissipation (blue, left column) and shelf sea dissipation (red, right column) plotted against GMSL for the constituents M_2, S_2, K_1 and O_1 (top to bottom). Circular makers show dissipation from the ICE-6G simulations, Gowan simulations are shown with crosses, and squares plot dissipation from the uniform SL runs (M_2 and K_1 only). Regression lines are plotted in black (solid for ICE-6G and dashed for uniform SL runs). The correlation coefficients r between the explicitly modelled and regression-estimated dissipation values are printed in each panel for ICE-6G (r_I), the uniform SL simulations (r_U), and the Gowan simulations (r_G). Stars indicate that the correlation is significant at the 99% confidence level.

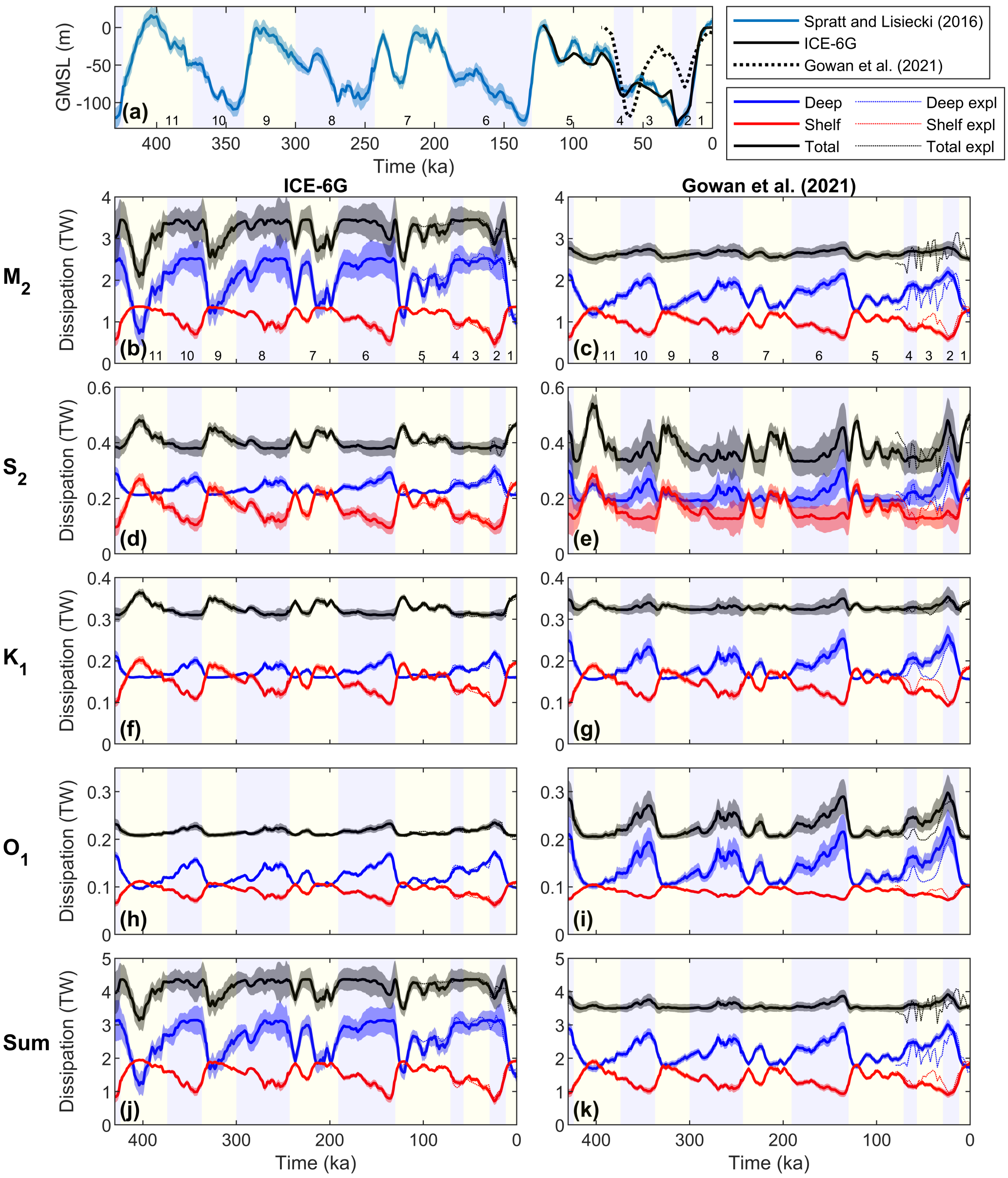

Figure 9. (a) Global mean sea level from the Spratt and Lisiecki (2016) reconstruction (blue line) with shading indicating upper and lower uncertainties, from the ICE-6G bathymetry (black solid line) and from Gowan et al. (2021) (black dotted line). Light blue and light yellow shading with corresponding numbering indicates Marine Isotope Stages. (b, d, f, h, j) Regression estimated dissipation for the constituents M_2, S_2, K_1 and O_1, respectively, and the sum thereof. Open ocean (deep) dissipation is plotted in blue, shelf sea dissipation in red and globally integrated dissipation in black using the ICE-6G regression models. Shading indicates one standard deviation uncertainty of the dissipation estimates. Explicitly modelled dissipation values for the last glacial cycle are overlain in with dashed lines. Light blue and light yellow shading with corresponding numbering indicates Marine Isotope Stages. (c, e, g, i, j, k) same as (b, d, f, h, j) but for the Gowan et al. (2021) regression model.

References

Anandakrishnan, S. (2003). Ice stream D flow speed is strongly modulated by the tide beneath the Ross Ice Shelf. *Geophysical Research Letters*, *30*(7), 1–4. doi: 10.1029/2002GL016329

Anselin, J., Reed, B. C., Jenkins, A., & Green, J. A. (2023). Ice Shelf Basal Melt Sensitivity to Tide-Induced Mixing Based on the Theory of Subglacial Plumes. *Journal of Geophysical Research: Oceans*, *128*(4), e2022JC019156. doi: 10.1029/2022JC019156

Arbic, B. K., Karsten, R. H., & Garrett, C. (2009). On tidal resonance in the global ocean and the back-effect of coastal tides upon open-ocean tides. *Atmosphere-Ocean*, *47*, 239–266. doi: 10.3137/OC311.2009

Arbic, B. K., MacAyeal, D. R., Mitrovica, J. X., & Milne, G. A. (2004). Ocean tides and Heinrich events. *Nature*, *432*(7016), 460. doi: 10.1038/432460a

Arbic, B. K., Mitrovica, J. X., MacAyeal, D. R., & Milne, G. A. (2008). On the factors behind large Labrador Sea tides during the last glacial cycle and the potential implications for Heinrich events. *Paleoceanography*, *23*, PA3211, doi:10.1029/2007PA001573.

Argus, D. F., Peltier, W. R., Drummond, R., & Moore, A. W. (2014). The Antarctica component of postglacial rebound model ICE-6G_C (VM5a) based on GPS positioning, exposure age dating of ice thicknesses, and relative sea level histories. *Geophysical Journal International*, *198*(1), 537–563. doi: 10.1093/gji/ggu140

Batchelor, C. L., Margold, M., Krapp, M., Murton, D.. K.., Dalton, A.. S., Gibbard, P.. L., Stokes, C.. R., Murton, J.. B. , . . . Manica, J. A. (2019). The configuration of Northern Hemisphere ice sheets through the Quaternary. *Nature communications*, *10*(1), 3713–110. doi: 10.1038/s41467-019-11601-2

Batchelor, C. L., Christie, F. D., Ottesen, D., Montelli, A., Evans, J., Dowdeswell, E. K., . . . Dowdeswell, J. A. (2023). Rapid, buoyancy-driven ice-sheet retreat of hundreds of metres per day. *Nature 2023 617:7959*, *617*(7959), 105–110. doi: 10.1038/s41586-023-05876-1

Bindschadler, R. a., King, M. a., Alley, R. B., Anandakrishnan, S., & Padman, L. (2003). Tidally controlled stick-slip discharge of a West Antarctic ice. *Science (New York, N.Y.)*, *301*(5636), 1087–9. doi: 10.1126/science.1087231

Carless, S. J., Green, J. A., Pelling, H. E., & Wilmes, S. B. (2016). Effects of future sea-level rise on tidal processes on the Patagonian Shelf. *Journal of Marine Systems*, *163*, 113–124. doi: 10.1016/j.jmarsys.2016.07.007

Clark, P. U., Dyke, A. S., Shakun, J. D., Carlson, A. E., Clark, J., Wohlfarth, B., . . . McCabe, A. M. (2009). The Last Glacial Maximum. *Science*, *325*(5941), 710–4. doi: 10.1126/science.1172873

Creveling, J. R., Mitrovica, J. X., Clark, P. U., Waelbroeck, C., & Pico, T. (2017). Predicted bounds on peak global mean sea level during marine isotope stages 5a and 5c. *Quaternary Science Reviews*, *163*, 193–208. doi: https://doi.org/10.1016/j.quascirev.2017.03.003

Dalton, A. S., Finkelstein, S. A., Barnett, P. J., & Forman, S. L. (2016). Constraining the Late Pleistocene history of the Laurentide Ice Sheet by dating the Missinaibi Formation, Hudson Bay Lowlands, Canada. *Quaternary Science Reviews*, *146*, 288–299. doi: 10.1016/j.quascirev.2016.06.015

Dalton, A. S., Pico, T., Gowan, E. J., Clague, J. J., Forman, S. L., McMartin, I., . . . Helmens, K. F. (2022). The marine δ18O record overestimates continental ice volume during Marine Isotope Stage 3. *Global and Planetary Change*, *212*, 103814. doi: 10.1016/j.gloplacha.2022.103814

De Boer, B., Lourens, L. J., & Van De Wal, R. S. (2014). Persistent 400,000-year variability of antarctic ice volume and the carbon cycle is revealed throughout the plio-pleistocene. *Nature Communications*, *5*(1), 1–8. doi: 10.1038/ncomms3999

Egbert, G. D. (2004). Numerical modeling of the global semidiurnal tide in the present day and in the last glacial maximum. *Journal of Geophysical Research*, *109*(C3), 1–15. doi: 10.1029/2003JC001973

Egbert, G. D., Bills, B. G., & Ray, R. D. (2004). Numerical modeling of the global semidiurnal tide in the present day and in the last glacial maximum. *Journal of Geophysical Research*, *109*(C3), 1–15. doi: 10.1029/2003JC001973

Ferrari, R., & Wunsch, C. (2009, jan). Ocean Circulation Kinetic Energy: Reservoirs, Sources, and Sinks. *Annual Review of Fluid Mechanics*, *41*(1), 253–282. doi: 10.1146/annurev.fluid.40

.111406.102139

Fox-Kemper, B., Helene T. Hewitt, Cunde Xiao, Guðfinna Aðalgeirsdóttir, Sybren S. Drijfhout, Tamsin L. Edwards, ... et al. (2021). Ocean, Cryosphere and Sea Level Change. In *Climate change 2021: The physical science basis. contribution of working group i to the sixth assessment report of the intergovernmental panel on climate change* (pp. 1211–1362).

Gomez, N., Weber, M. E., Clark, P. U., Mitrovica, J. X., & Han, H. K. (2020). Antarctic ice dynamics amplified by Northern Hemisphere sea-level forcing. *Nature 2020 587:7835*, *587*(7835), 600–604. doi: 10.1038/s41586-020-2916-2

Gowan, E. J., Zhang, X., Khosravi, S., Rovere, A., Stocchi, P., Hughes, A. L. C., ... Lohmann, G. (2021). A new global ice sheet reconstruction for the past 80.000 years. *Nature Communications*, *12*(1), 1199. doi: 10.1038/s41467-021-21469-w

Grant, K. M., Rohling, E. J., Bronk Ramsey, C., Cheng, H., Edwards, R. L., Florindo, F., ... Williams, F. (2014). Sea-level variability over five glacial cycles. *Nature Communications*, *5*(1), 1–9. doi: 10.1038/ncomms6076

Green, J. A. (2010). Ocean tides and resonance. *Ocean Dynamics*, *60*(5), 1243–1253. doi: 10.1007/s10236-010-0331-1

Green, J. A., & Huber, M. (2013). Tidal dissipation in the early Eocene and implications for ocean mixing. *Geophysical Research Letters*, *40*(11), 2707–2713. doi: 10.1002/grl.50510

Green, J. A., Huber, M., Waltham, D., Buzan, J., & Wells, M. (2017). Explicitly modelled deep-time tidal dissipation and its implication for Lunar history. *Earth and Planetary Science Letters*, *461*, 46–53. doi: 10.1016/j.epsl.2016.12.038

Green, J. A. M., & Nycander, J. (2013). A Comparison of Tidal Conversion Parameterizations for Tidal Models. *Journal of Physical Oceanography*, *43*(1), 104–119. doi: 10.1175/JPO-D-12-023.1

Griffiths, S. D., & Peltier, W. R. (2008). Megatides in the Arctic Ocean under glacial conditions. *Geophysical Research Letters*, *35*, L08605, doi:10.1029/2008GL033263.

Griffiths, S. D., & Peltier, W. R. (2009). Modeling of polar ocean tides at the Last Glacial Maximum: amplification, sensitivity, and climatological implications. *Journal of Climate*, *22*, 2905–2924. doi: 10.1175/2008JCLI2540.1

Gudmundsson, G. H. (2007). Tides and the flow of Rutford Ice Stream, West Antarctica. *J. Geophys. Res.*, *112*(F4), F04007. doi: 10.1029/2006JF000731

Hayden, A. M., Wilmes, S. B., Gomez, N., Green, J. A., Pan, L., Han, H., & Golledge, N. R. (2020). Multi-Century Impacts of Ice Sheet Retreat on Sea Level and Ocean Tides in Hudson Bay. *Journal of Geophysical Research: Oceans*, *125*(11), e2019JC015104. doi: 10.1029/2019JC015104

Hendershott, M. C. (1972). The effects of solid earth deformation on global ocean tides. *Geophysical Journal of the Royal Astronomic Society*, *29*, 389–402.

Kendall, R. A., Mitrovica, J. X., & Milne, G. A. (2005). On post-glacial sea level – II. Numerical formulation and comparative results on spherically symmetric models. *Geophysical Journal International*, *161*(3), 679–706. doi: 10.1111/J.1365-246X.2005.02553.X

Lambeck, K. (2004). Sea-level change through the last glacial cycle: geophysical, glaciological and palaeogeographic consequences. *Comptes Rendus Geoscience*, *336*(7), 677–689. doi: https://doi.org/10.1016/j.crte.2003.12.017

Lambeck, K., Rouby, H., Purcell, A., Sun, Y., & Sambridge, M. (2014). Sea level and global ice volumes from the Last Glacial Maximum to the Holocene. *Proceedings of the National Academy of Sciences of the United States of America*, *111*(43), 15296–15303. doi: 10.1073/pnas.1411762111

Menviel, L., Timmermann, A., Elison Timm, O., & Mouchet, A. (2017). Deconstructing the Last Glacial termination: the role of millennial and orbital-scale forcings. *Quaternary Science Reviews*, *30*(9–10), 1155–1172. doi: 10.1016/j.quascirev.2011.02.005

Milillo, P., Rignot, E., Mouginot, J., Scheuchl, B., Morlighem, M., Li, X., & Salzer, J. T. (2017). On the Short-term Grounding Zone Dynamics of Pine Island Glacier, West Antarctica, Observed With COSMO-SkyMed Interferometric Data. *Geophysical Research Letters*, *44*(20), 10,436–10,444. doi: 10.1002/2017GL074320

Milne, G. A., & Mitrovica, J. X. (1996). Postglacial sea-level change on a rotating Earth: first results from a gravitationally self-consistent sea-level equation. *Geophysical Journal International*, *126*(3), F13–F20. doi: 10.1111/j.1365-246X.1996.tb04691.x

Mitrovica, J. X., & Milne, G. A. (2003). On post-glacial sea level: I. General theory. *Geophysical Journal International*, *154*(2), 253–267. doi: 10.1046/J.1365-246X.2003.01942.X

Olinger, S. D., Lipovsky, B. P., Wiens, D. A., Aster, R. C., Bromirski, P. D., Chen, Z., . . . Stephen, R. A. (2019). Tidal and Thermal Stresses Drive Seismicity Along a Major Ross Ice Shelf Rift. *Geophysical Research Letters*, *46*(12), 6644–6652. doi: 10.1029/2019GL082842

Peltier, W. R., Argus, D. F., & Drummond, R. (2015). Space geodesy constrains ice age terminal deglaciation: The global ICE-6G-C (VM5a) model. *Journal of Geophysical Research: Solid Earth*, *120*(1), 450–487. doi: 10.1002/2014JB011176

Pickering, M. D., Horsburgh, K. J., Blundell, J. R., Hirschi, J. J., Nicholls, R. J., Verlaan, M., & Wells, N. C. (2017). The impact of future sea-level rise on the global tides. *Continental Shelf Research*, *142*, 50–68. doi: 10.1016/j.csr.2017.02.004

Pico, T., Mitrovica, J. X., Ferrier, K. L., & Braun, J. (2016). Global ice volume during MIS 3 inferred from a sea-level analysis of sedimentary core records in the Yellow River Delta. *Quaternary Science Reviews*, *152*, 72–79. doi: 10.1016/j.quascirev.2016.09.012

Pico, T., Creveling, J. R., & Mitrovica, J. X. (2017). Sea-level records from the U.S. mid-Atlantic constrain Laurentide Ice Sheet extent during Marine Isotope Stage 3. *Nature Communications*, *8*(1), 1–6. doi: 10.1038/ncomms15612

Pöppelmeier, F., Jeltsch-Thömmes, A., Lippold, J., Joos, F. , & Stocker, T.. F. (2023). Multi-proxy constraints on Atlantic circulation dynamics since the last ice age. *Nature Geosciences*, *16*, 349–356. doi: 10.1038/s41561-023-01140-3

Ray, R. D., Rowlands, D. D., & Egbert, G. D. (2003). Tidal models in a new era of satellite gravimetry. *Space Science Reviews*, *108*, 271–282.

Rohling, E. J., Grant, K., Bolshaw, M., Roberts, A. P., Siddall, M., Hemleben, C., & Kucera, M. (2009). Antarctic temperature and global sea level closely coupled over the past five glacial cycles. doi: 10.1038/ngeo557

Schaffer, J., Timmermann, R., Erik Arndt, J., Savstrup Kristensen, S., Mayer, C., Morlighem, M., & Steinhage, D. (2016). A global, high-resolution data set of ice sheet topography, cavity geometry, and ocean bathymetry. *Earth System Science Data*, *8*(2), 543–557. doi: 10.5194/essd-8-543-2016

Schmittner, A., Green, J. A., & Wilmes, S. B. (2015). Glacial ocean overturning intensified by tidal mixing in a global circulation model. *Geophysical Research Letters*, *42*(10), 4014–4022. doi: 10.1002/2015GL063561

Shakun, J. D., Lea, D. W., Lisiecki, L. E., & Raymo, M. E. (2015). An 800-kyr record of global surface ocean δ18O and implications for ice volume-temperature coupling. *Earth and Planetary Science Letters*, *426*, 58–68. doi: 10.1016/j.epsl.2015.05.042

Siddall, M., Rohling, E. J., Almogi-Labin, A., Hemleben, C., Meischner, D., Schmelzer, I., & Smeed, D. A. (2003). Sea-level fluctuations during the last glacial cycle. *Nature*, *423*(6942), 853–858. doi: 10.1038/nature01690

Simpson, J. H., & Pingree, R. D. (1978). Shallow sea fronts produced by tidal stirring. In *Oceanic fronts in coastal processes: Proceedings of a workshop held at the marine sciences research center, may 25–27, 1977* (pp. 29–42).

Spada, G., & Stocchi, P. (2007). SELEN: A Fortran 90 program for solving the "sea-level equation". *Computers & Geosciences*, *33*(4), 538–562. doi: 10.1016/J.CAGEO.2006.08.006

Spratt, R. M., & Lisiecki, L. E. (2016). A Late Pleistocene sea level stack. *Climate of the Past*, *12*(4), 1079–1092. doi: 10.5194/cp-12-1079-2016

Sulzbach, R., Klemann, V., Knorr, G., Dobslaw, H., Dümpelmann, H., Lohmann, G., & Thomas, M. (2023). Evolution of global ocean tide levels since the Last Glacial Maximum. *Paleoceanography and Paleoclimatology*, *38*, e2022PA004556. doi: 10.1029/2022PA004556

Thomas, H., Bozec, Y., Elkalay, K., & de Baar, H. J. W. (2004). Enhanced open ocean storage of CO2 from shelf sea pumping. *Science (New York, N.Y.)*, *304*(5673), 1005–8. doi: 10.1126/science.1095491

Uehara, K., Scourse, J. D., Horsburgh, K. J., Lambeck, K., & Purcell, A. P. (2006). Tidal evolution of the northwest European shelf seas from the Last Glacial Maximum to the present. *Journal* *of Geophysical Research*, *111*, C09025, doi: 10. 1029/2006JC003531.

Velay-Vitow, J., Peltier, W. R., & Stuhne, G. R. (2020). The Tides of the Glacial Ocean and Their Possible Connection to Heinrich Event Instabilities of the Laurentide Ice Sheet. *Journal of Geophysical Research: Oceans*, *125*(1). doi: 10.1029/2019JC015444

Waelbroeck, C., Labeyrie, L., Michel, E., Duplessy, J. C., McManus, J. F., Lambeck, K., ... Labracherie, M. (2002). Sea-level and deep water temperature changes derived from benthic foraminifera isotopic records. *Quaternary Science Reviews*, *21*(1), 295–305. doi: https://doi.org/10.1016/S0277-3791(01)00101-9

Walker, R. T., Parizek, B. R., Alley, R. B., Anandakrishnan, S., Riverman, K. L., & Christianson, K. (2013). Ice-shelf tidal flexure and subglacial pressure variations. *Earth and Planetary Science Letters*, *361*, 422–428. doi: 10.1016/J.EPSL.2012.11.008

Ward, S. L., Neill, S. P., Scourse, J. D., Bradley, S. L., & Uehara, K. (2016). Sensitivity of palaeotidal models of the northwest European shelf seas to glacial isostatic adjustment since the Last Glacial Maximum. *Quaternary Science Reviews*, *151*, 198–211. doi: https://doi.org/10.1016/j.quascirev.2016.08.034

Wilmes, S. B., & Green, J. A. (2014). The evolution of tides and tidal dissipation over the past 21,000 years. *Journal of Geophysical Research: Oceans*, *119*(7), 4083–4100. doi: 10.1002/2013JC009605

Wilmes, S. B., Green, J. A., Gomez, N., Rippeth, T. P., & Lau, H. (2017). Global Tidal Impacts of Large-Scale Ice Sheet Collapses. *Journal of Geophysical Research: Oceans*, *122*(11), 8354–8370. doi: 10.1002/2017JC013109

Wilmes, S.-B., Green, J. A. M., & Schmittner, A. (2021). Enhanced vertical mixing in the glacial ocean inferred from sedimentary carbon isotopes. *Communications Earth & Environment*, *2*(1), 166. doi: 10.1038/s43247-021-00239-y

Wilmes, S. B., Schmittner, A., & Green, J. A. (2019). Glacial Ice Sheet Extent Effects on Modeled Tidal Mixing and the Global Overturning Circulation. *Paleoceanography and Paleoclimatology*, *34*(8), 1437–1454. doi: 10.1029/2019PA003644

Wilmes, S. B., Ward, S., & Uehara, K. (2022). Present day: Tides in a changing climate. In *A journey through tides* (pp. 185–229). Elsevier. doi: 10.1016/B978-0-323-90851-1.00009-1

Wilmes, S. B., Pedersen, V. K., Schindelegger, M., & Green, J. A. (2023). Late Pleistocene evolution of tides and tidal dissipation: tidal simulations [Dataset]. *Zenodo*. doi: 10.5281/zenodo.8147509

Wunsch, C., & Ferrari, R. (2004). Vertical mixing, energy, and the general circulation of the oceans. *Annual Review of Fluid Mechanics*, *36*, 281–314, doi:10. 1146/annurev. fluid. 36. 050802.

Zaron, E. D., & Egbert, G. D. (2006). Estimating open-ocean barotropic tidal dissipation: The Hawaiian Ridge. *Journal of Physical Oceanography*, *36*, 1019–1035.